Mine Water and the Environment (2019) 38:226–242
https://doi.org/10.1007/s10230-019-00603-7

TECHNICAL ARTICLE

Groundwater Recharge Assessment in an Arid, Coastal, Middle Mountain Copper Mining District, Coquimbo Region, North-central Chile

Jorge Oyarzún[1] · Jorge Núñez[1,2] · Jerry P. Fairley[3] · Sebastián Tapia[4] · Diana Alvarez[5] · Hugo Maturana[1,10] · José Luis Arumí[6,7] · Evelyn Aguirre[8] · Alfonso Carvajal[1] · Ricardo Oyarzún[1,7,9]

Received: 22 December 2017 / Accepted: 8 March 2019 / Published online: 16 March 2019

Abstract
Groundwater recharge processes operating in a portion of the western slope of the Chilean Coastal Cordillera (30°S) were assessed. The study takes advantage of the presence of the Cerro Brillador Mine (CBM), currently part of the Universidad de La Serena mining research center. Six factors—slope, solar exposure, drainage density, lineament density, geology and vegetation were characterized in a 12 km × 12 km area around the mine to identify the zones of greatest and least potential for groundwater recharge. The analysis indicates that approximately 66% of the total area presents favorable conditions for recharge. At a more local scale, the work focused on the CBM itself, an experimental facility where structural measurements in the interior and exterior of the mine, monitoring of the water level in the shaft, and sampling of mine water for chemical and isotopic composition were carried out. The chemical analysis highlighted the lack of acid drainage, despite the existence of pyrite (FeS_2) and copper-sulfate mineralization in the mine. The isotopic analysis showed that the groundwater has a similar signature to local precipitation. From this information, a simple conceptual model for the hydrogeology is proposed, in which precipitation rapidly recharges the mine along faults and joints with a preferential N-S strike, but is impounded by the Urrutia fault, which facilitates the storage of groundwater in the underground workings by acting as a flow barrier. A simple analysis suggests a recharge rate on the order of 5% of the average annual precipitation for the CBM area.

Keywords Groundwater infiltration · Hydrogeology · Mountain-block recharge · Cerro Brillador Mine · GIS

Introduction

Opportunities to directly study mountain-block-scale hydrogeological processes are limited, due to the difficulty of making in-situ observations within rock masses, where access is necessarily restricted. The primary venues for making such observations have been underground laboratories, often operated by government agencies for the purpose of carrying out particle physics experiments or for studying problems such as the safe geologic disposal of high-level

✉ Ricardo Oyarzún
royarzun@userena.cl

[1] Departamento Ingeniería de Minas, Universidad de La Serena, La Serena, Chile

[2] Centro del Agua para Zonas Aridas y Semiáridas de América Latina y el Caribe, La Serena, Chile

[3] Department of Geological Sciences, University of Idaho, Moscow, USA

[4] Ingeniería Civil Ambiental, Universidad de La Serena, La Serena, Chile

[5] Ingeniería de Ejecución en Minas, Universidad de La Serena, La Serena, Chile

[6] Departamento de Recursos Hídricos, Universidad de Concepción, Concepción, Chile

[7] Centro de Recursos Hídricos para la Agricultura y Minería (CRHIAM), Concepción, Chile

[8] Comisión Chilena de Energía Nuclear (CCHEN), Las Condes, Chile

[9] Centro de Estudios Avanzados en Zonas Áridas (CEAZA), La Serena, Chile

[10] Escuela de Prevención de Riesgos y Medio Ambiente, Universidad Católica del Norte, Coquimbo, Chile

nuclear waste. A great deal of progress has been made in understanding infiltration, deep percolation, fracture flow, and water–rock interactions with the access provided by these underground laboratories. Examples include the Mizunami underground research laboratory in Japan (Iwatsuki et al. 2005), the Gran Sasso underground laboratory in Italy (e.g., Adinolfi et al. 2008), the Atomic Energy of Canada Limited's Underground Research Laboratory in Manitoba, and the Exploratory Studies Facility at Yucca Mountain, Nevada, in the United States of America (Cizdziel et al. 2008). Despite the value of observations and experiments at these facilities, the costs of maintenance and operation are high, causing many valuable facilities to close. For example, the Underground Research Laboratory of Manitoba was closed in 2003 and the Exploratory Studies Facility at Yucca Mountain was forced to cease operations in 2010 due to funding constraints.

To continue underground observations and experiments in an era of shrinking funding, investigators have turned to using underground workings instead of dedicated scientific facilities. For example, the Aberdeen Tunnel Underground Laboratory is a particle physics laboratory, opportunistically located between two vehicular tubes (the Aberdeen Tunnel) on the Island of Hong Kong. Another example is the Sanford Laboratory, the former Homestake gold mine in South Dakota, USA, which was also turned into a particle physics research facility. Similar to these examples, other transportation tunnels and old or operational mine workings, can also offer unique opportunities to study hydrological subsurface processes, including infiltration, deep percolation, fracture flow, and species transport.

A case in point is the Cerro Brillador Mine (CBM), located on the western slope of the Coastal Cordillera zone in north-central Chile. In colonial times, the CBM supplied the first Chilean copper exports, which were shipped to Peru at the request of the Viceroyalty, so it has an important historical value. Significant production persisted throughout the nineteenth century (Maksaev et al. 2007), and the area still contains economic ore reserves. The mine continued to operate sporadically until 2014. Currently, the mine workings constitute the Experimental and Training Center for Mining of the Universidad de La Serena, where two galleries at 500 and 580 m above sea level (masl) are used for the instruction of mining and engineering students and for observations and experiments in groundwater flow and transport in low-permeability, fractured rock. To the best of our knowledge, the CBM is the only facility of its kind in Latin America.

Despite the arid climate in the CBM area (Squeo et al. 2006), the existence of permanent mine flooding below 480 masl and continuous seepage in several areas of the accessible workings provide evidence of a steady recharge of deep percolating groundwater. Thus, both the mine area in general and the underground levels in particular, offer a natural laboratory to study groundwater recharge processes and flow in arid zones with shallow soils and underlying fractured rock masses. Within this context, the current work aims to: (1) obtain a potential recharge map in a 12 km × 12 km area surrounding the CBM, based on landscape factors analysis within a GIS environment, and (2) characterize the source and controls on deep percolation in this portion of the mountainous middle-inland rain-fed dryland of the Coquimbo Region in a complementary, more detailed scale using the CBM workings.

Study Area

Brillador District

The geomorphology of the Brillador District is typical of the western Coastal Cordillera of the Norte Chico (Paskoff 1993). The physiography of the region is dominated by a chain of hills, ranging in elevation from 500 to 800 masl in the area of the CBM, and to over 1000 masl in other locations. The landscape is bisected by Santa Gracia Gulch and the Elqui River Valley (Fig. 1). Toward the west, steep-sided hills give way to a gentle piedmont at 300 masl and a lower terrace averaging 150 masl. A coastal terrace and beach areas, with an average elevation of about 10 masl, form the western boundary between the region and the Pacific Ocean. This relief presents a drainage pattern of steep-sided gorges, predominantly oriented toward the west. Toward the east, the hills have elevations of 300–800 masl with gentler slopes and drain toward the Santa Gracia Gulch.

The zone has a steppe climate with abundant cloud cover. The average annual temperature is 13.6 °C, while the average maximum and minimum temperatures are 18.9 °C and 11.2 °C, respectively (Araya and Salfate 2014). Average annual precipitation is approximately 90 mm, and potential evapotranspiration exceeds 1000 mm year^{-1}. The gulches and creeks are normally dry, with the exception of small springs that have minimal flows. However, surface water runoff is normally observed during the El Niño years, in association with the sharp increase in precipitation that usually accompanies the phenomenon.

The CBM

The CBM is located between 200 and 750 masl on the southern face of Cerro Brillador, which reaches a maximum height of 1034 masl. The deposit is representative of several other vein-type deposits of Jurassic and Cretaceous age located in the Coastal Cordillera of North Chile. Although the deposits had no more than hundreds of thousands or few million tons of ore, their high grades resulting from natural secondary enrichment processes allowed early mining

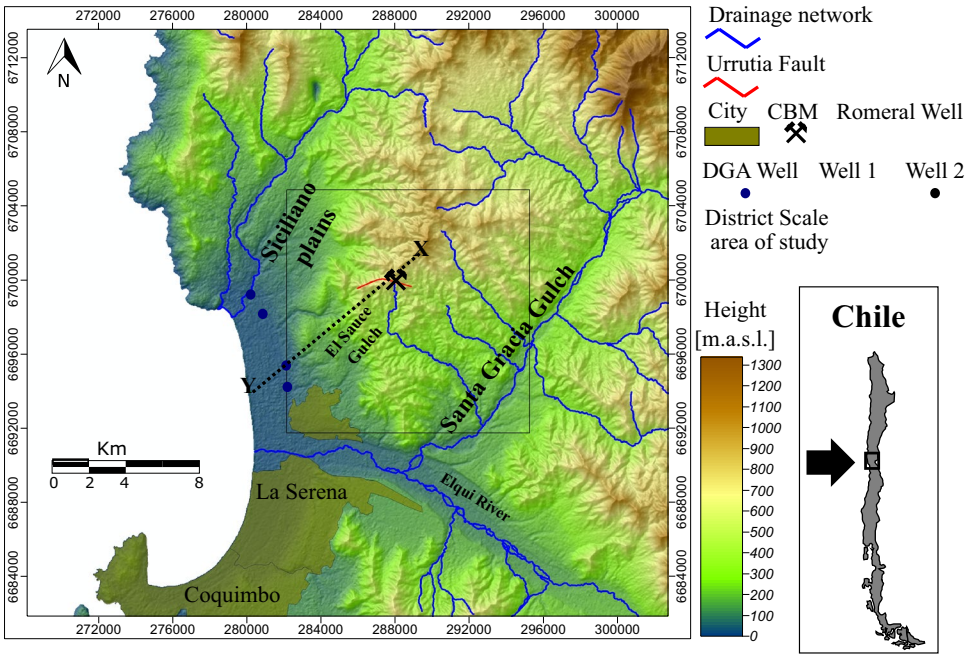

Fig. 1 Location and main geomorphological features of the study area

of oxidized ores and later the smelting of the rich sulfides (4–16% Cu) in a reverberatory furnace.

According to Llaumett (1970), the CBM comprises two subparallel lode veins separated by 20–30 m and controlled by a major fault (the Urrutia fault), which is a steeply-dipping (65ºS) normal fault that strikes N70ºW. The veins extended for 120–130 m in the upper levels and for 60 m at the 200-m level. The thickness of the ore bodies varies but does not exceed 9 m. The mineralogy of the veins includes: pyrite and chalcopyrite ($CuFeS_2$) with bornite (Cu_5FeS_4) and chalcocite (Cu_2S) as secondary sulfides, and oxidized copper minerals, such as chalcanthite ($Cu(SO_4)\cdot 5H_2O$) and chrysocolla ($(Cu,Al)_2H_2Si_2O_5(OH)_4\cdot nH_2O$). The veins are hosted in andesitic rocks that have undergone contact metamorphism, with chloritic alteration and silicification. The upper 70 m of the veins contained oxidized ores, underlain by rich sulfides with bornite to a depth of 540 masl; further below, chalcopyrite dominated. The host rock is cut by porphyritic andesite and rhyodacite dikes that strike between N70ºW and N60°E. There are also secondary faults with infilling of 0.5–12 cm. The dominant strike of these faults is N20°W–N10°E (coinciding with the strike of the joint sets), with secondary strikes of N20°–30°E and N70°–90°W.

As consequence of long-term mining, underground workings in the CBM reached the 200 (masl) level. However, most of these workings are currently buried or flooded. An open-pit mine was developed in recent decades, and its operation ceased in 2014. The pit is located approximately above the center of the underground mine, slightly (about 30 m) to the NE, and above the 620 level (Fig. 2). Its upper diameter is approximately 150 m. The two main underground levels that are not flooded or clogged are located at 580 and 500 masl (from here onwards, 580 and 500 levels, respectively), oriented approximately parallel to a surface ravine, or "quebrada," trending N20ºE on the same south-facing slope as the mine portals (Fig. 2). The 580 and 500 levels trend N20ºE and N38ºE, and are 120 and 350 m long, respectively. A vertical shaft connects the two and intersects the water table *ca*. 20–25 m below the 500 level invert (Fig. 2). The lower levels were described as being flooded more than 90 years ago by Kuntz (1925) and later by Dubo (1984), and they remain flooded. In years of high rainfall, water can reach the 500 level, and draining is required. At various times in the past, water has been pumped from the shaft for use in mineral processing. On the basis of early water withdrawal data described by Kuntz (1925), and subsequent information compiled by the current authors, the long-term, average flow rate of water into the shaft is approximately 0.3 l s^{-1}.

Materials and Methods

As stated by Shelp et al. (2011), "a rational approach to water resource investigation includes the use of common sense and as many independent sources of information as possible, including historical information, ground-based investigation, and remote sensing." This approach is followed in the current work, which considered investigations at two scales of analysis, i.e. at the district and mine scale.

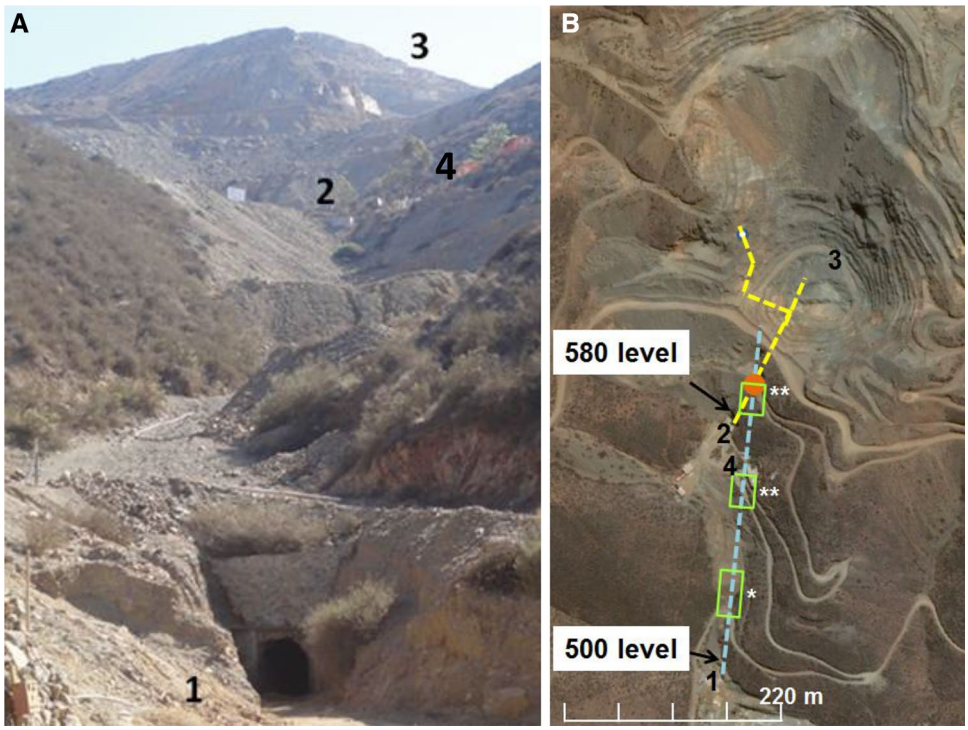

Fig. 2 Photograh (**a**) and Google Earth plan view (**b**) of the CBM area. A shows the 500 m level adit (1), the 580-m level access zone and camp (2), the open-pit area (3), and the camp facilities (4). **b** The location of the vertical shaft (orange circle) that connects the 580 and 500 levels, the dripping zone recorded in 2016 (single asterisk), and zones with evidence of recent water flow (double asterisk) in the 500 level

General Analysis of Potential Recharge Zones at the District Scale

A 12 km × 12 km area, approximately centered on the CBM and referred to in this study as "district-scale", was defined. Using remote sensing and GIS, thematic maps of landscape features were developed to provide an indication of potential infiltration zones, following an approach similar to Singh et al. (2013).

Information Sources and Processing

Spectral bands in the visible and NIR channels of the Landsat 5 satellite and its TM sensor, and the Landsat 7 satellite and its ETM + sensor, were used. In addition, we employed a 30 m × 30 m resolution digital elevation model (DEM) created by the Japan Space System with information captured by the ASTER sensor and obtained from the U.S. Geological Survey (USGS) EarthExplorer server. Processing of the satellite images and the DEM was carried out with the System for Automated Geoscientific Analyses (SAGA) GIS (Conrad et al. 2001). GeoTiff Examiner (Mentor Software Inc.) was used for the correction of the false northing effect of the conventional Landsat coordinates system. All raster layers were projected in UTM WGS84 Zone 19. The satellite images were calibrated radiometrically converting Landsat Digital Numbers (DN) to at-sensor spectral radiance according to Chander et al. (2009):

$$L_l = G_{\text{rescale}} \times Q_{\text{cal}} + B_{\text{rescale}}, \quad (1)$$

$$\text{where}: \; G_{rescale} = \frac{LMAX_\lambda - LMIN_\lambda}{Q_{calmax} - Q_{calmin}}, \quad (2)$$

$$B_{\text{rescale}} = \text{LMIN}_{\lambda -} \left(\frac{\text{LMAX}_\lambda - \text{LMIN}_\lambda}{Q_{\text{calmax}} - Q_{\text{calmin}}} \right) Q_{\text{calmin}}, \quad (3)$$

and L_λ is the spectral radiance at the sensor's aperture [W $(m^2\ sr\ \mu m)^{-1}$]; Q_{cal} is the quantized calibrated pixel value (DN); Q_{calmin} and Q_{calmax} correspond to the minimum and maximum quantized calibrated pixel value corresponding to $LMIN_\lambda$ (DN); $LMIN_\lambda$ and $LMAX_\lambda$ are the spectral at-sensor radiance scaled to Q_{calmin} and Q_{calmax} [W $(m^2\ sr\ \mu m)^{-1}$]; $G_{rescale}$ is the band-specific rescaling gain factor [(W $(m^2\ sr\ \mu m)^{-1}$) DN^{-1}]; and $B_{rescale}$ is the band-specific rescaling bias factor [W $(m^2\ sr\ \mu m)^{-1}$].

Atmospheric correction was performed using the COST method (Chavez 1996):

$$R_\lambda = \frac{\pi \times d^2 \times \left(L_\lambda - L_{\text{haze}}\right)}{E_{\text{SUN}_\lambda} \times \cos(\theta)}, \quad (4)$$

where R_λ is the surface reflectance; d is the distance between the Earth and the sun (AU); L_{haze} is the path radiance; E_{SUN_λ} is the exo-atmospheric solar irradiance; and θ corresponds to the sun zenith angle (or 90 − sun elevation angle). Likewise, the images were corrected topographically using the Minnaert (1941) procedure according to (Smith et al. 1980):

$$R_{\lambda_c} = \frac{R_\lambda \times \cos(e)}{\cos^k i \times \cos^k e}, \quad (5)$$

where R_{λ_c} is the topographically corrected surface reflectance; i is the Solar incidence angle, and e is the effective view angle.

Slope and slope orientation layers were obtained by conventional terrain analysis procedures (Bachmair and Weiler 2012) implemented in the "terrain analysis morphometry" module available in SAGA GIS (Conrad et al. 2015). In the case of slope, four categories were defined: 0°–12° (lowest potential runoff and thus most favorable for the recharge), 12.5°–25°, 25°–37.5°, and > 37.5° (greatest potential runoff and least favorable for recharge). For slope orientation, and in agreement with Montecinos (1982) and the location of the study area at 30°S latitude, exposures of 90°–180° (with respect to 0° North) were considered the most favorable for moisture storage (due to receiving less solar radiation), while slopes with exposures between 270° and 360° represent the most unfavorable (greatest incident solar radiation, greatest potential evapotranspiration). Exposure ranges of 45°–90° and 180°–225° were considered "good," while the intervals 0°–45° and 225°–270° were defined as "moderate", in terms of infiltration and recharge potential relative to received radiation, and therefore, evapotranspiration losses.

Prassad et al. (2008), Shaban et al. (2006), and Smith et al. (1997) suggest that greater drainage densities are associated with greater surface runoff potential, and therefore less infiltration (and recharge). In this context, the drainage network was determined following the recommendations of Hengl et al. (2010), based on the deterministic eight nodes (D8) algorithm proposed by O'Callaghan et al. (1984), which assumes that a water particle in each DEM cell flows toward one and only one of its neighboring cells, which is the one in the direction of steepest descent (Zhao et al. 2009). The drainage network, in vector format, was subsequently converted to raster format with a pixel size of 15 m × 15 m. The cell values were encoded to represent the presence/absence of a segment of the drainage network in a given cell by a 1 or 0, respectively. To transform the binary coding to a continuous variable, the grid resolution was reduced to 75 m × 75 m per cell, which represents the sum of the values of the 25 15 m × 15 m component cells. The sum was mapped back onto the 15 m × 15 m grid using B-Spline interpolation (Lee et al. 1997). The result of this transform was a drainage density layer at 15 m × 15 m resolution, expressed in m m^{-2}.

The main lithological units of the study area were obtained from the geologic map (at scale 1:100,000) N° 18 La Serena-La Higuera (Emparán and Pineda 2000), which was georeferenced and digitized. The different units were grouped into four classes associated with recharge potential, considering their formation environment and the presence of materials with high infiltration rates, such as sand and gravel (Table 1).

The basic premise linking lineament density and recharge is that zones with greater lineament density possess a higher degree of fracturing of the underlying rock stratum, and therefore have a greater potential for recharge (Prassad et al. 2008). To obtain the lineament densities, data on the major features included in the work of Emparán and Pineda (2000) was complemented by semi-automatic extraction based on the spectral bands of Landsat 7. The RGB 321 (natural color) and RGB 543 (false color) bands, which have been proposed as suitable for such purposes in previous studies (Ciren 2004; Dar et al. 2010; Prassad et al. 2008) were considered. The images were improved using "contrast enhancement" techniques through the Color Restoration Step of the Multiscale Retinex algorithm (Petro et al. 2014), as well as a Difference of Gaussian filter (Assitari et al. 2014), for which the GIMP2 software was used. The linear attributes identified (in both the geologic map and from the semi-automatic extraction) were digitized and coded as a binary variable (i.e. 0 or 1 for absence or presence, respectively). The resulting binary lineation map was transformed to a continuous variable lineation density map using a procedure equivalent to that used for the drainage density layer.

Finally, we considered vegetation as indicative of infiltration and ultimately potential recharge, under the assumption that zones in which infiltration is more frequent and/or there is greater shallow subsurface water storage should exhibit greater and more permanent plant cover. To quantify this effect, we used the NDVI (normalized difference vegetation index) according to Matsushita et al. (2007) and Rouse et al. (1974):

$$\mathrm{NDVI} = \frac{\rho_{\mathrm{nir}} - \rho_{\mathrm{red}}}{\rho_{\mathrm{nir}} + \rho_{\mathrm{red}}}, \quad (6)$$

Table 1 Lithologic classes

Class	Lithology
1	Alluvial deposits, old and recent fluvial deposits, aeolian deposits, Coquimbo formation (conglomerates)
2	Hydrothermal alteration zones, Arqueros formation (volcanic sequence with fossiliferous calcareous sandstone)
3	Arqueros formation (volcanic sequence with marine sediment intercalations)
4	Intrusive granitoids and contact-metamorphic rocks of the Arqueros Formation

where ρ_{red} is the reflectance at the red (0.6–0.7 μm) wavelength, and ρ_{nir} corresponds to the reflectance at the near-infrared (NIR) (0.7–1.1 μm) wavelength.

Satellite images from four dates were considered: Dec. 2001, Jan. 2003, Jan. 2009, and Dec. 2010. These dates were selected on the basis of scene availability, with the objective of including images of the summer period for a year in which the previous winter had been rainy. In particular, it was decided to calculate both the NDVI average and standard deviation in the study area based on the four selected images (Tweed et al. 2007). The average NDVI for the different dates was assumed to be an indicator of the health status of the vegetation (i.e. how green it was); thus, the greater the water availability in the area, the higher the NDVI (Shaban et al. 2006). The NDVI standard deviation was in turn considered to be an indicator of the permanence of the vegetation. That is, if the NDVI of an area had a high standard deviation, it was inferred that the vegetation is highly variable from year to year, likely due to the absence of more permanent subsurface water storage. In other words, the water is rather ephemeral and intermittent. Using this approach, four vegetation compound index (VCI) classes were defined in accordance with the average NDVI values and standard deviations (Table 2).

Integration of Thematic Layers for the Recharge Potential Map

The integration of the different thematic layers was carried out using simple GIS algebra (i.e. values of each factor for a given cell were summed). We followed Singh et al. (2013) in assigning equivalent weights to each factor. Table 3 presents a summary of the ranges and scores assigned to each thematic layer (attribute).

Table 2 Vegetation compound index (VCI) classes determined as a function of the averages NDVI and standard deviations for the study area and the four dates considered

	NDVI average	
	Low	High
NDVI standard deviation		
High	Class 3: Meadow—seasonal low-structure vegetation	Class 2: Scrubland—seasonal medium-structure vegetation
Low	Class 4: Desert—little cover, normally dry	Class 1: Forest—always wet, highest-structure vegetation

Table 3 Ranges and scores for the different attributes (thematic layers)

Thematic layer	Range	Units	Score
Slope	0–12.5	Degrees	40
	12.5–25		30
	25–37.5		20
	> 37.5		10
Solar exposure	90–180	Degrees from due north	40
	180–225		30
	225–270		20
	270–360		10
Drainage density	0–0.0125	$m\ m^{-2}$	40
	0.0125–0.0250		30
	0.0250–0.0375		20
	0.0375–0.05		10
Lineament density	0–0.02	$m\ m^{-2}$	40
	0.02–0.04		30
	0.04–0.06		20
	0.06–0.08		10
Geology	Class 1	n/a	40
	Class 2		30
	Class 3		20
	Class 4		10
Vegetation	Class 1	CVI	40
	Class 2		30
	Class 3		20
	Class 4		10

Characterization of Water Source and Flow Mechanisms in the CBM

To investigate the migration of recharge between the near-surface and the water table, the second stage of the work considered a detailed study of hydrogeological aspects for the CBM.

Geological-Structural Characterization and Identification of Areas with Water Presence

The characterization of geology and structural features involved detailed work in the interior of the CBM, especially at the 500 level, as well as work outside the mine (i.e. along surface access roads). From May 2015 to July 2016, we completed detailed descriptions and mapping of the locations, strikes, and dips of the fractures and faults in and around the CBM. In total, 257 and 125 observations of faults and fractures were made in the interior (500 level) and exterior of the mine (near the 580 level entrance), respectively. In addition, the locations of dripping water in the 500 level were identified in a way that allowed them to be

related to both the geological information and the locations of the CBM installations at the 580 level. The dataset was processed with DIPS 5.041 software (Rocscience). To complete the geological-structural information for the site, we augmented the data obtained from our work in the 500 level with the detailed mapping of Zambra (2015), carried out at the 580 level, to obtain a comprehensive synthesis of the CBM geology and structure.

Dynamics and Characteristics of Water in the Interior of the CBM

We evaluated water level fluctuations and determined isotopic and chemistry characteristics for groundwater in the CBM. To measure changes in the potentiometric surface elevations, we installed a TROLL 500 water level logger in the vertical shaft connecting the 500 and 580 levels. The logger was placed ≈ 10 m below the water level in the shaft, ≈ 20 m below the floor of the 500 level. The sensor was first installed in May 2014, and water level measurements at a sampling frequency of once every 6 h were available for May to Nov. 2014 and May 2015 to Nov. 2016.

The stable isotope (^{2}H, ^{18}O) data were collected during three time periods. The first set of samples was collected in July 2006 in the 500 level, at a location where water drips from the ceiling, and from two wells, one 3 km SE and the other 2 km NE of the CBM (Fig. 1). In the second sampling campaign, undertaken in Nov. 2015, water samples were taken from the shaft and from the dripping features on the 500 level ceiling. Finally, similar samples were obtained in August 2016. In addition, samples were collected of domestic water at the mine facilities center and from a rainwater collector installed close to the 580 level entrance. For the latter, it was possible to collect three samples in 2015, corresponding to the rainfall that occurred in autumn and winter (April–September), and one sample in 2016 (a particularly dry year, with only one precipitation event of more than 10 mm recorded between the months of April and October). Isotopic analyses of the 2006 and 2015 samples were performed at the Environmental Isotope Laboratory of the Chilean Nuclear Energy Commission (CCHEN), while those collected in 2016 were analyzed at the University of Waterloo-Environmental Isotope Laboratory (uwEILAB) in Canada. The 2006 samples were analyzed using a Finnigan MAT 252 isotope ratio mass spectrometer, whereas those of 2015 and 2016 were processed using a liquid water stable isotope analyzer (Los Gatos Research, CA, USA). Isotope ratios are expressed in per mil (‰) using the usual δ notation:

$$\delta(‰) = \left[\left(R_{sample} - R_{standard}\right)/R_{standard}\right] \times 1000, \quad (7)$$

where R refers to either the $^{2}H/^{1}H$ or $^{18}O/^{16}O$ ratio of a sample and the standard (Vienna Standard Mean Ocean Water, VSMOW), respectively. Analytic errors for ^{18}O and ^{2}H at CCHEN were 0.1 and 1‰, respectively, for the 2006 samples and 0.08 and 1‰, for those from 2015. Likewise, analytical errors from the uwEILAB for the 2016 samples were 0.2 and 0.8‰ for ^{18}O and ^{2}H, respectively.

Finally, given that pyrite is an abundant primary mineral at the CBM, and conditions are favorable for its oxidation in the mine works, the presence of acid drainage was expected. In fact, in the 580 level there are abundant oxidized mineral stalactites, as well as small pools with green (copper) or brown (iron) coloration that reach a pH of 2. However, these features are rather rare in the 500 level. Thus, for purposes of characterizing the chemical composition of the shaft water, we sampled it in August 2016 (composite sample), and again in October 2016 (multi-level samples, at 2, 5, and 10 m depths; an obstruction in the shaft prevented additional sampling at greater depths). In addition to pH and electric conductivity (EC) measurements, Ca, Mg, Na, K, Fe, Cu, and Mn were determined by atomic absorption spectrometry; As was determined by hydride generation; HCO_3 and Cl using the volumetric method; and SO_4 by gravimetry (Rice et al. 2012).

Results and Discussions

General Characterization of Potential Recharge Zones (District Scale)

The slope of the hillsides affects recharge by influencing water accumulation and infiltration; the steeper the slope, the greater the surface runoff, which decreases the potential for infiltration. The dominant slope (52% of the total study area) ranges from 0 to 12.5%. In contrast, the "most unfavorable" class (in terms of potential for recharge), with slopes of 37.5°–50°, covers ≈ 1% of the study area, mostly to the north, northwest, and west of the CBM (Fig. 3a). In terms of slope orientation (Fig. 3b), the areas most (i.e. 90°–180°) and least favorable for recharge (i.e. 270°–360°) each occupy about 23% of the study area. The intermediate categories (exposures oriented 0°–90°, 180°–225°, and 225°–270°) account for the rest, covering 54% of the total.

The lower the density of streams, the greater the potential for groundwater recharge. Drainage density (Fig. 3c) in the 0–0.125 m m^{-2} range is considered most favorable for potential water recharge and is strongly dominant, covering 77% of the study area. The most unfavorable class (0.0375–0.050 m m^{-2}) represents only 1% of the study area and is concentrated mostly northwest and east of the CBM site.

Unconsolidated lithologies are more favorable for recharge than unweathered bedrock. Class 1 lithologies (fluvial and alluvial deposits) cover 35% of the total study

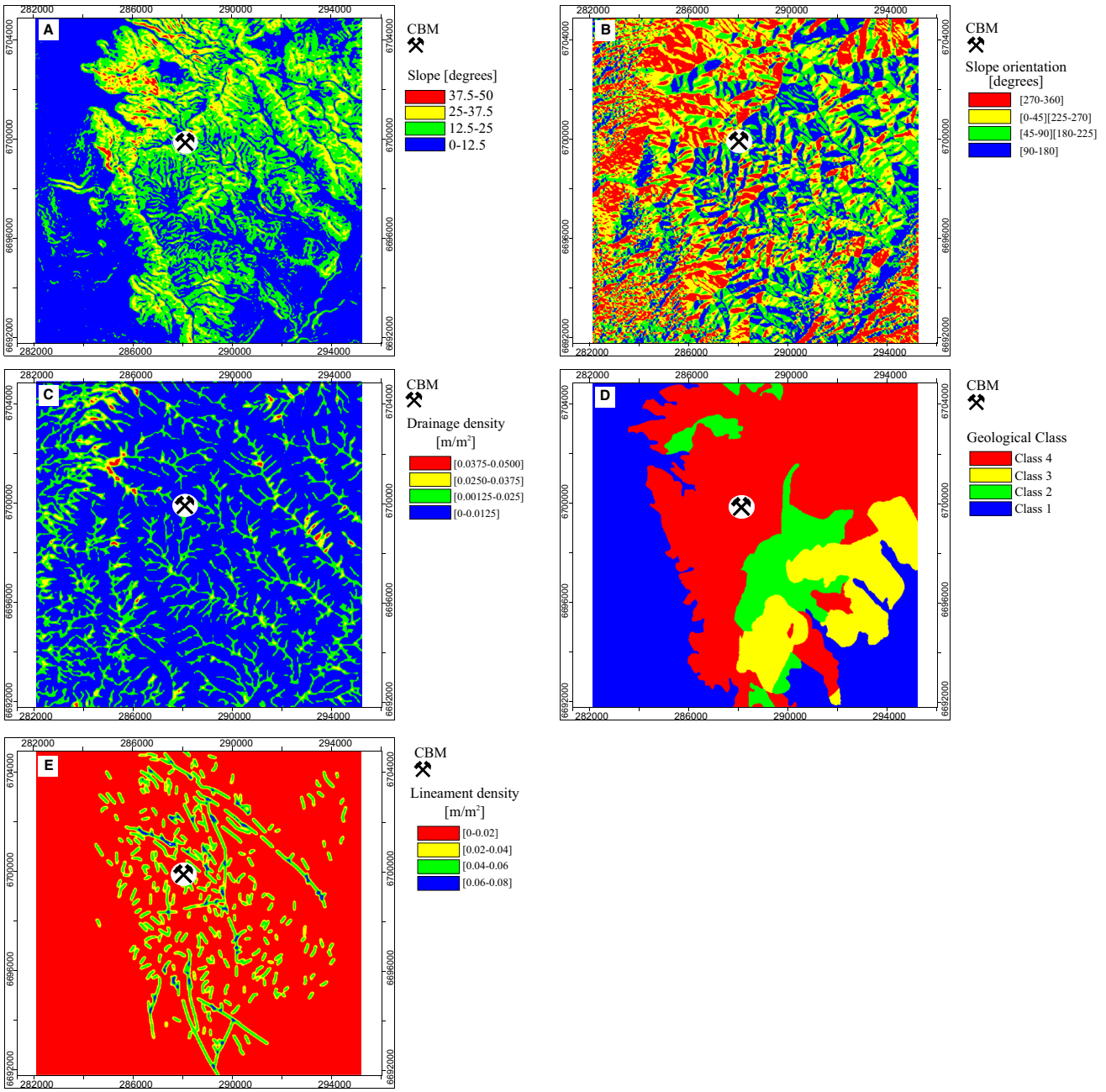

Fig. 3 Spatial distribution of landscape features: slope angle (**a**), slope orientation (**b**), drainage density (**c**), lithology (**d**), and lineament density (**e**). Lithological classes are fluvial and alluvial deposits (1), volcanic sequence with fossiliferous calcareous sandstone (2), volcanic sequence with marine sediment intercalations (3) and intrusive granitoids and contact-metamorphic andesites (4)

area. Class 4 lithologies (intrusive granitoids and contact-metamorphic andesites) account for 44% of the study area (Fig. 3d). The remaining 21% of the study area is distributed between lithology Classes 2 (a volcanic sequence with fossiliferous calcareous sandstone) and 3 (a volcanic sequence with marine sediment intercalations).

Figure 3e presents the lineament density. Although this factor is treated as a separate attribute, it should be noted that linear features (e.g. joints, faults) are not completely independent of rock type. Despite the possible correlation between lineament density and lithology, high lineament density favors infiltration, and the possibility of adding information on infiltration potential not entirely captured by the lithology attribute argued strongly for its retention in the analysis. The 0–0.02 m m^{-2} range, which is the least favorable for water infiltration and recharge, dominates the distribution, covering 85% of the total study area.

The most favorable range for infiltration and recharge, 0.06–0.08 m m^{-2}, encompasses only 1% of the study area.

For vegetative cover (Fig. 4), the percent of the study area covered by VCI Classes 1, 2, 3, and 4 (see Table 2 for definitions) were rather similar, at 21, 29, 21, and 29%, respectively (Fig. 4c). Disregarding agricultural fields in the southeast corner of the study area, the greatest mean NDVI values are concentrated in the central part of the study area (Fig. 4a). A noticeable visual relationship was evident between the distribution of the NDVI standard deviation (Fig. 4b) and lineament density (Fig. 3e). A Chi squared test of the binned values of lineament density and NDVI standard deviation indicated that the two variables cannot be considered independent (p value = 0.0005). In fact, the Pearson's linear correlation test rejected the null hypothesis that the two variables were uncorrelated with a high degree of significance (p value < 2.2E−16). Presumably, the association between variability in vegetative cover (i.e. NDVI standard deviation) and lineament density reflects the spatially discrete nature of fractures. Our assumption is that high permeability, low storage flow pathways (lineaments and fractures) rapidly remove precipitation from the near surface, while unfractured and lower permeability areas with higher near-surface storage capacity may hold infiltration in the shallow soil cover for longer periods of time, creating high spatial variability in the availability of water and thus vegetative cover.

We integrated the values of the six attributes (thematic layers) on a pixel-by-pixel basis to obtain an integrated distributed recharge potential map for the study area (Fig. 5). Since each attribute had a maximum score of 40 (for the class most favorable in terms of recharge potential), the maximum possible score for each map cell is 240. We divided the scores into four bins, or classes, each of 60 points (i.e. Class 1 greater than or equal to 0 and less than 60, Class 2 is greater than or equal to 60 and less than 120, etc.). These categories were designated "very low," "low," "moderate," and "high," respectively. More than half the study area (62.6%) was classified as having moderate recharge potential. For the remaining overall recharge potential categories, 0.4% of the area had very low recharge potential, while 32.7% had low, and 4.2% had high recharge potential.

Hydrogeological Characterization of the CBM

Geological-Structural Characteristics

Figure 6 presents a rose diagram of the orientation of structural features identified in the present study, inside (at the 500 level) and outside of the mine. In general, a good correspondence was observed between the orientations on structural control in the two environments, with discontinuities striking NW-SE predominating (especially inside the mine). It was also observed that the zones in the 500 level with active mineral drippings or evidence of recent dripping (e.g. inferred from the presence of limonitic efflorescences) were associated with structures having a N70°W strike as well. The spatial orientation of fractures determined in the current work is in good agreement with observations made by Zambra (2015) at the 580 level. The dominant strikes of the faults are between N20ºW and N10ºE, with dips from 50° to 60°W, and their openings, ranging from 0.5 to 12 cm, are filled with gauge material. A separate group of faults is oriented sub-parallel to the major Urrutia fault, with strikes of N80°–84°W and dips on the order of 50° to the SW or NW. The apertures of the joints generally range from 0.1 to 5 mm, and their dominant fill is limonite with minor amounts of gypsum.

Water Presence and Dynamics

Although there are zones of dripping water in the 500 level (Fig. 2) near the mine facilities (in a vertical projection), other zones further away also have dripping water. The spatial distribution of these zones suggests that the dripping observed in the 500 level is not likely related to the use of water and its disposal (wastewater) at the mine camp (i.e. restroom, dining room), an impression that is strengthened by the responsiveness of dripping and water levels in the vertical shaft to rainfall events, as well as isotopic signatures, as described below.

Figure 7 presents the water level variation in the vertical shaft from May to Dec. 2014 and May 2015 to Nov. 2016. It highlights a rapid and direct response of the water level to "major" precipitation events, in particular those greater than 20 or 25 mm of rainfall per day. For example, the rain event of 11–12 June 2014, consisting of 22 mm of precipitation, increased the water level in the shaft by almost 10 cm. Similarly, water level increases on the order of 15 cm were associated in 2015 with the precipitation events of 12–13 July (35 mm) and 14 Oct. (29 mm). Although the "rapid and immediate response" associated with these rainfall events is likely due to preferential flow through fractures, a second response of the water level to precipitation is also observed, particularly after the events of June 2014 and July 2015. Following those two events, there is a slower but sustained rise in water levels that appears to be due to diffuse flow, or delayed recharge (as opposed to the rapid recharge observed immediately in connection with major precipitation events). Similar behavior was described by Squeo et al. (2006), who monitored a nearby well (Romeral) that taps the alluvial deposit of the Romeral Gorge, some 8 km NW of the CBM, at an altitude of ≈160 masl (Fig. 1). They state that "… the Romeral aquifer responded very fast to recharge events associated with rains over the average value for the precipitation in the study area" and "…local precipitation plays a

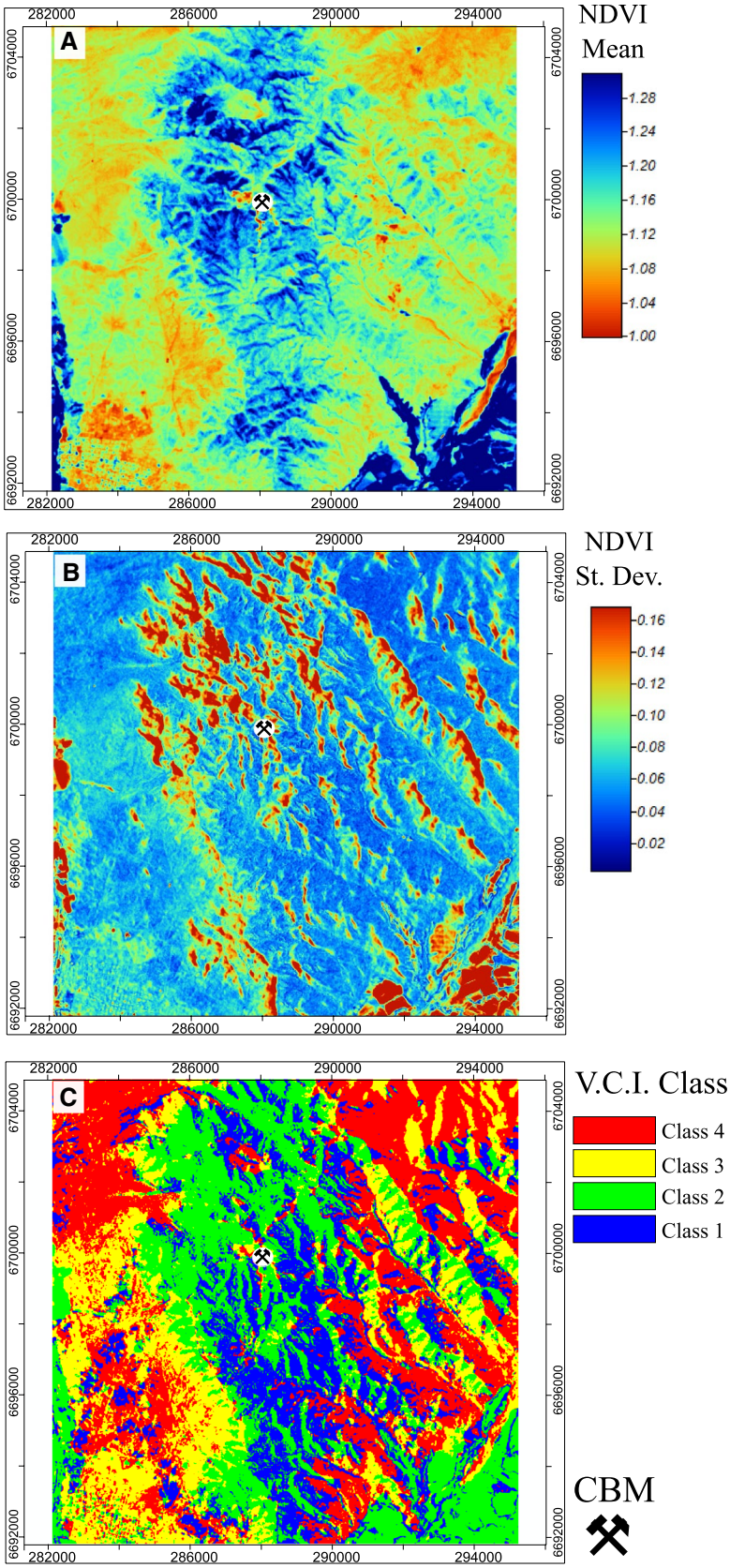

Fig. 4 Spatial distribution of vegetative cover: average normalized difference vegetation index, NDVI (**a**), NDVI standard deviation (**b**) and vegetation compound index, VCI (**c**). VCI classes are always wet, highest-structure vegetation (1); scrubland—seasonal medium-structure vegetation (2); meadow—seasonal low-structure vegetation (3); and desert—little cover, normally dry (4)

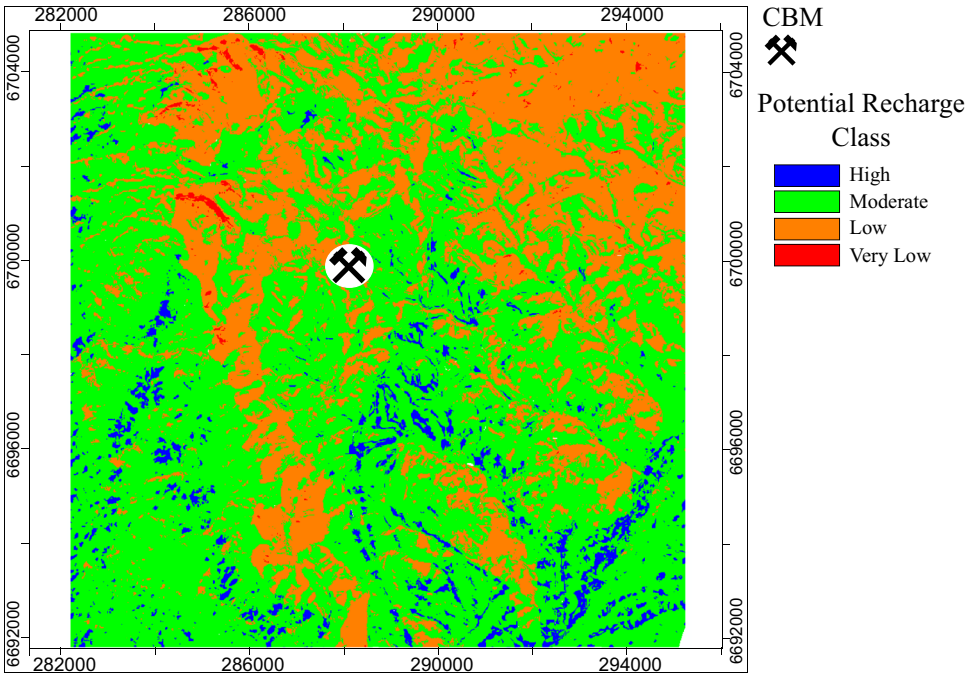

Fig. 5 Spatial distribution of recharge potential in the study area. High: 196–240; moderate: 151–195; low: 106–150; very low: 60–105

significant role in groundwater recharge", which is consistent with the observations at the CBM. The combination of high permeability pathways for infiltration and limited storage at the land surface offers a plausible explanation.

On the other hand, two major water level declines were associated with seismic events. A co-seismic drop in water levels of > 20 cm was associated with a magnitude 8.4 earthquake that struck the Coquimbo region in Sept. 2015, and a similar, but lower magnitude, co-seismic drop accompanied the magnitude 6.9 aftershock of 11 Nov. 2015. It has been known at least since the 1960s that water levels in wells react to both near-field and teleseismic stress changes (e.g. Cooper et al. 1965), with the most common response being a co-seismic drop in the potentiometric surface, often followed by an exponential rise in water levels (e.g. Brodsky et al. 2003; King et al. 1999). Although the data taken from the CBM clearly indicate a co-seismic drop, evidence for post-seismic increases in water level is more ambiguous. In fact, water levels appear to follow a pattern of decline after the main earthquake in Sept. 2015, which was interrupted by the storm event of Oct. 2015 (29 mm; Fig. 7).

Isotopic and Water Chemistry Data

Table 4 presents the stable isotope signatures of the sampled water sources. In an earlier investigation, Squeo et al. (2006) reported values between −9 and −2‰ for $\delta^{18}O$ and −77 to −10 for $\delta^{2}H$ for precipitation at the Romeral meteorological station, with a weighted average of −4.8 for $\delta^{18}O$ and −28.1 for $\delta^{2}H$. The Romeral meteorological station is located 8 km NW of the CBM, next to the aforementioned Romeral well. Values from the Romeral meteorological station are, in general, similar to those obtained near the CBM (Table 4).

Delta values (both for ^{2}H and ^{18}O) for water samples obtained inside the mine are similar to those for local rainwater, reinforcing the local meteoric origin of recharge intercepted in the mine galleries. In addition, the isotopic composition of water sampled in the galleries shows no sign of mixing with water imported for the mine camp activities, providing independent confirmation that dripping water in the CBM is not related to the surface facilities located at the 580 level. In summary, the isotopic evidence strongly supports the conclusion that water in the galleries and vertical shaft of the CBM is sourced entirely from infiltration/percolation, originating as local precipitation.

The water in the vertical shaft (below the 500 level) has a pH of 6.7. Despite the effect of pyrite oxidation and the presence of copper-sulfate minerals in the mine, acid drainage is not an important process. The neutral pH is presumably due to the neutralizing effect of the chloritized mafic andesitic host rock, an effect that has been observed in other deposits hosted by mafic rocks with chloritic alteration in the Coquimbo region (Oyarzun et al. 2007). No calcite is present in the veins, and carbonate reaction to HCl is weak and scattered in both the 580 and 500 levels. Compositionally, the water sampled from the shaft is essentially Ca–SO_4 brackish water that does not exhibit significant vertical stratification with depth. On average, the major components are: Ca: 600 mg L^{-1}, Mg: 253 mg L^{-1}, Na: 252 mg L^{-1}, K: 5 mg L^{-1}, SO_4: 2220 mg L^{-1}, Cl: 698 mg L^{-1}, and HCO_3: 272 mg L^{-1}, with an EC of 4.6 dS m^{-1}. The solution is also rich in Cu (1.2 mg L^{-1}), and contains As (0.1 mg L^{-1}), Mn

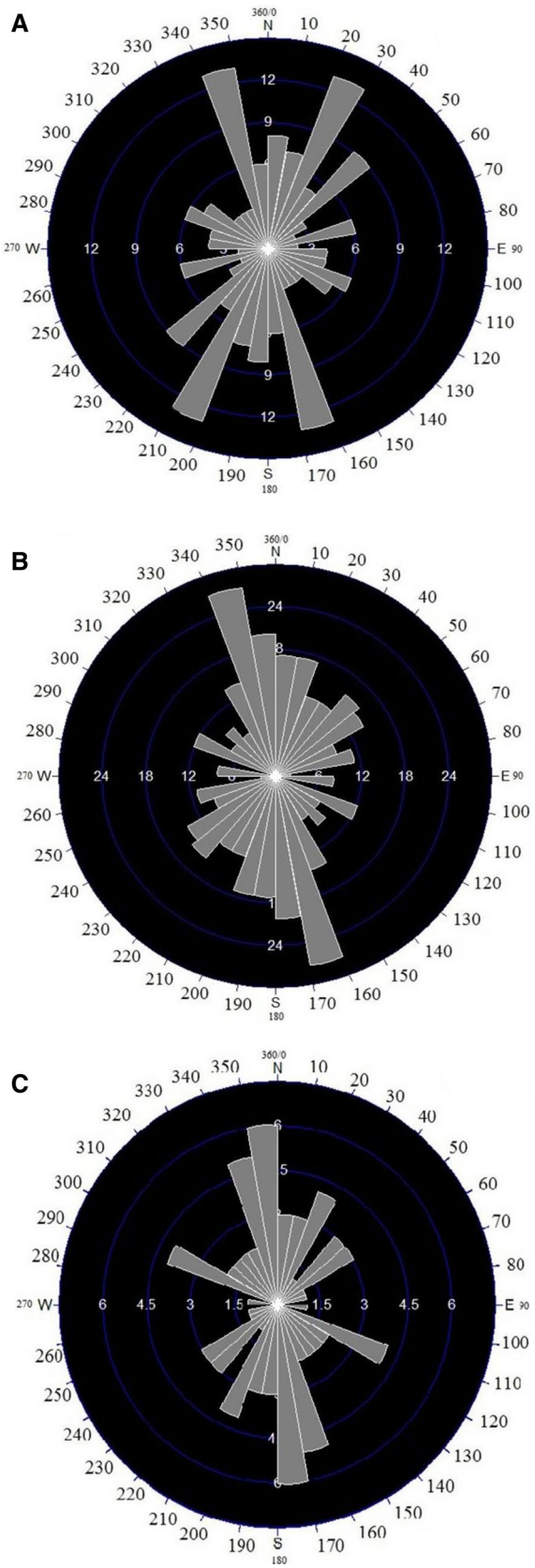

Fig. 6 Rose diagram of faults and joints. **a** Outside the CBM, access road near the 580 level; **b** inside the CBM, 500 level; **c** similar to **b**, but restricted to sections with active or recent drippings

(0.86 mg L^{-1}), and Fe (0.23 mg L^{-1}). This composition is consistent with neutralization of sulfuric acid by minerals that release Ca, Mg, and Na.

Integrated Analysis

Using the information presented above, a simple conceptual model of the most important hydrogeological processes operating in the mountain block setting of the study area was developed, as discussed below.

Source of Recharge

The stable isotope data indicate that that the source of recharge in the CBM is local rainfall. Large magnitude precipitation events are associated with increased groundwater levels in the vertical shaft of the CBM. The transport of infiltrated rainfall water through the vadose zone appears to occur preferentially through fractures with a dominant N–S orientation; however, major cross-cutting features (such as the Urrutia fault) may influence flow paths in the vadose zone and/or impound significant groundwater in the saturated zone. Considering the variety of fracture fills and the range of apertures associated with the faults and joints in the rock mass, it is reasonable to expect a relatively wide range of infiltration and flow velocities. This expectation receives anecdotal support from observations of staggered timing in the onset of dripping at locations in the CBM galleries following precipitation events.

Discharge Area

Although direct evidence of the primary discharge zones for aquifers in the study area is lacking, the proximity of the CBM site to the coast (on the order of 6–10 km) argues that the coastal plain aquifers are the likely recipients of groundwater that infiltrates in the mountain block regions. Historical information from four Chilean Water Authority monitoring wells (Dirección General de Aguas, DGA), located 2 km from the coast (Fig. 1), established that the elevation of the water table in the coastal aquifers was about 8–10 masl. While the CBM may locally modify groundwater flow patterns, it is possible to assume that on a wider scale, the water table in the rock massif should follow the slope of the terrain (Babiker and Gudmundsson 2004; Buchtele et al. 2003). Thus, groundwater sourced from infiltration in the mountain block is assumed to migrate from higher elevations to the E, S, and especially W, through terraced surfaces at ≈150 masl (El Siciliano, Juan Soldado, and La Compañía plains) and feed the coastal aquifer (Fig. 8).

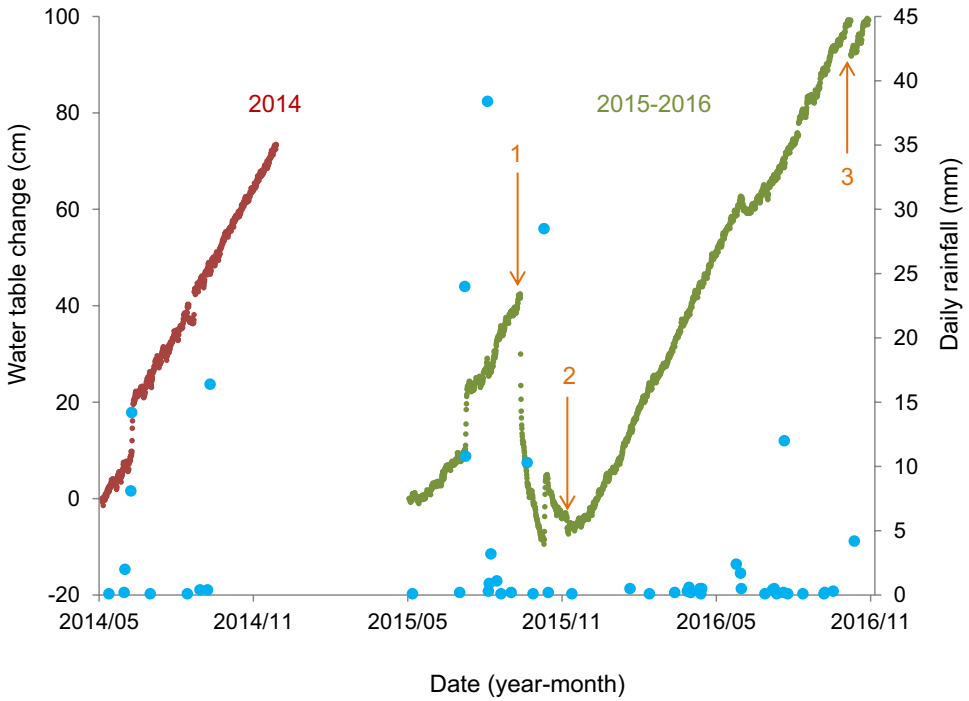

Fig. 7 Water level variation in the shaft and rainfall for the period of study. Water levels are in centimeters of deviation from the initial value recorded at the beginning of each period May–December 2014 (red dots, start date May 2014), and May 2015–November 2016 (green dots, start date May 2015); positive values indicate increases in water level from the start dates, while negative values correspond to lower water level with respect to the initial measurement. Rainfall data (blue dots) were obtained from CEAZA-MET (Romeral station, available at http://www.ceazamet.cl/index.php?pag=mod_estacion&e_cod=5). Specified events: (1) magnitude 8.3 earthquake (16 September 2015); (2) magnitude 6.9 earthquake (11 November 2015); (3) water extraction from the shaft for chemical and isotope analysis (12 October 2016)

Table 4 Isotopic signatures of water samples

Year	Sample	δ^2H (‰)	$\delta^{18}O$ (‰)
2006	Gallery dripping[a] (500 m level, CBM)	− 40.5	− 5.3
	Well 1 (Los Placeres Creek)	− 42.6	− 5.6
	Well 2 (Maria Elena)	− 51.7	− 6.2
2015	Flooded shaft, CBM	− 30.0	− 5.12
	Gallery dripping (500 m level, CBM)	− 28.2	− 4.78
	Mine camp water	− 88.3	− 11.1
	Local rainfall[b]	− 31.4 (9.4)	− 5.5 (1.3)
2016	Flooded shaft, CBM[c]	− 32.3 (0.2)	− 5.2 (0.1)
	Gallery dripping (500 m level, CBM)	− 31.0	− 5.1
	Mine camp water[d]	− 100.1 (0.1)	− 13.1 (0.1)
	Local rainfall	− 30.3	− 5.1

[a]Average of two samples (dripping locations)

[b]Average (and standard deviation) of three rainfall events collected during July–November 2015

[c]Average (and standard deviation) of five samples collected from August to October 2016

[d]Average of two samples collected in July and October 2016 (locations of wells 1 and 2 in Fig. 1)

Mountain Block Permeability and Storage

The hydrologic conditions in the CBM argue for predominantly high secondary permeability, enhanced by the mine workings. The oxygen and deuterium isotopes show little evidence of fractionation associated with water–rock interaction. The lack of evidence for water–rock interaction and the rapid response of water levels to precipitation events in the CBM are consistent with transport by high-permeability fractures with low storage coefficients. Furthermore, the detritic type of soil covering is likely to encourage percolation to the fractured rock mass. The low storage potential in the fractured rock mass in the vadose zone is likely to extend below the local water table, increasing the sensitivity of the groundwater system to stresses arising from, for example, seismic events such as those observed in 2015.

Role of the Urrutia Fault

Investigations of exhumed paleofault exposures indicate that faults in the crystalline rock may form barriers or conduits to cross-fault groundwater flow, or a combination of these two (barrier/conduit) extremes (Caine et al. 1996). It

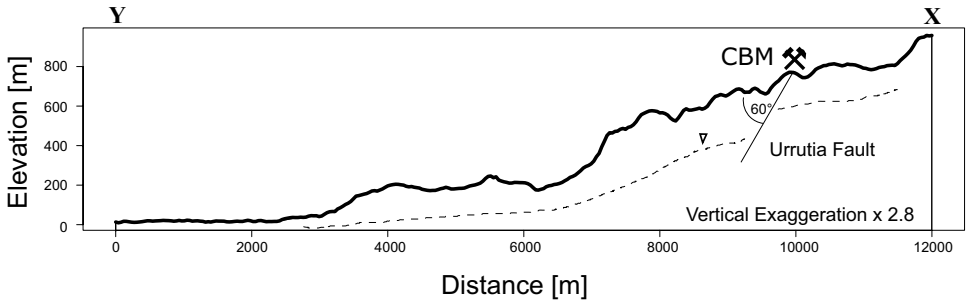

Fig. 8 E–W cross-section between points *X* and *Y* (see Fig. 1) and estimated water table configuration (dashed line; not to scale)

is well-known that the hydraulic architecture of a fault can evolve over time (Caine et al. 1996; Evans et al. 1997), and it is generally assumed that greater throw on a fault correlates with a well-developed, low permeability fault core. Thus, larger offset faults are more likely to act as barriers to flow. In the present case, it appears likely that the Urrutia fault, which strikes sub-normal to the topographical gradient in the mine area, and therefore, to the presumed flow direction (i.e. S–SW), acts as a barrier to flow and may intercept infiltration and migrating groundwater, helping to channel water into the mine workings through secondary faults and joints of preferential N–S strike. This inference is based on the fact that a fault typically disrupts the previous structural network of fracture connections in the rock massif, and being normal to the flow direction, it will not be an effective hydraulic channel. Based on the previous information, a simple conceptual model for the hydrogeology of the zone is proposed, in which rainfall rapidly recharges the mine along faults and joints with a preferential N–S strike and is impounded by the Urrutia fault, which facilitates the movement of groundwater to the underground workings by acting as a barrier to flow.

Recharge Rate Estimation

From our conceptual model and understanding of the attributes of the study area, we developed a rough estimate of the effective groundwater recharge rate in the vicinity of the CBM. Starting with the annual rainfall, we focused our consideration to areas above 500 masl, whose recharge effects could be observed in the galleries of the CBM. From the upstream area, we disregarded the zones corresponding to surface water flow in streams diverging with respect to CBM, assuming that shallow water flow paths follow surface topography. From these considerations, we estimated an effective recharge source area (polygon in Fig. 9) on the order of 2.5 km^2. Given that, as mentioned before, it is possible to estimate a long-term average groundwater flow rate into the mine of 0.3 L s^{-1} (or ca. 9460 m^3 $year^{-1}$), this allows us to determine a preliminary long-term average recharge of *ca*. 4 mm $year^{-1}$ (i.e. 9460 m^3 $year^{-1}$ divided by 2.5×10^6 m^2) or ca. 5% of annual total precipitation, a plausible value for semi-arid or arid zones (Scanlon et al. 2006).

Conclusions

A variety of complementary methods (remote sensing, observation of groundwater levels, water chemistry, and isotope data) were successfully integrated to understand mountain block hydrology in an arid, rain-fed coastal belt of north-central Chile. The study area was the CBM, a copper mine representative of vein-type deposits of Cretaceous age that were the basis of Chilean and world copper production in the nineteenth century.

In particular, the use of satellite information and freely available software allowed the zones of greatest recharge potential to be spatially characterized for a 12 km × 12 km area around the CBM. For this, topography, slope and slope orientation, drainage density, lineament density, geology, and vegetation were considered. On the basis of these thematic layers and their integration, a spatially distributed recharge potential indicator map was obtained. Approximately 66% of the total area presents favorable (i.e. moderate and high) recharge potential conditions.

At a more detailed scale, the collection and analysis of stable isotope data from water samples collected inside the CBM provided compelling evidence that the recharge is of local meteoric origin, and not related to the "imported" camp water. Monitoring of water levels in the CBM provided evidence of rapid response to significant rainfall events (e.g. over 20 mm day^{-1}), followed by a sustained but less rapid increase in water levels.

Observations indicate that areas of dripping water in the CBM underground workings are commonly associated with fractures striking N10°W, implying these features are optimally oriented in the local stress regime to transmit infiltrating fluids. The early arrival times of wetting fronts to the saturated zone, and the strong response of the water table to seismic events, implies that the fracture network presents high permeability but likely low storativity. The continued rise in water levels following major storm events indicates that the unsaturated fracture network does possess some capacity to buffer infiltration fronts, although the attenuation capacity of the crystalline rock mass is yet to be determined.

In contrast to the apparent transmissibility of the fracture network, the Urrutia fault, which strikes normal to the

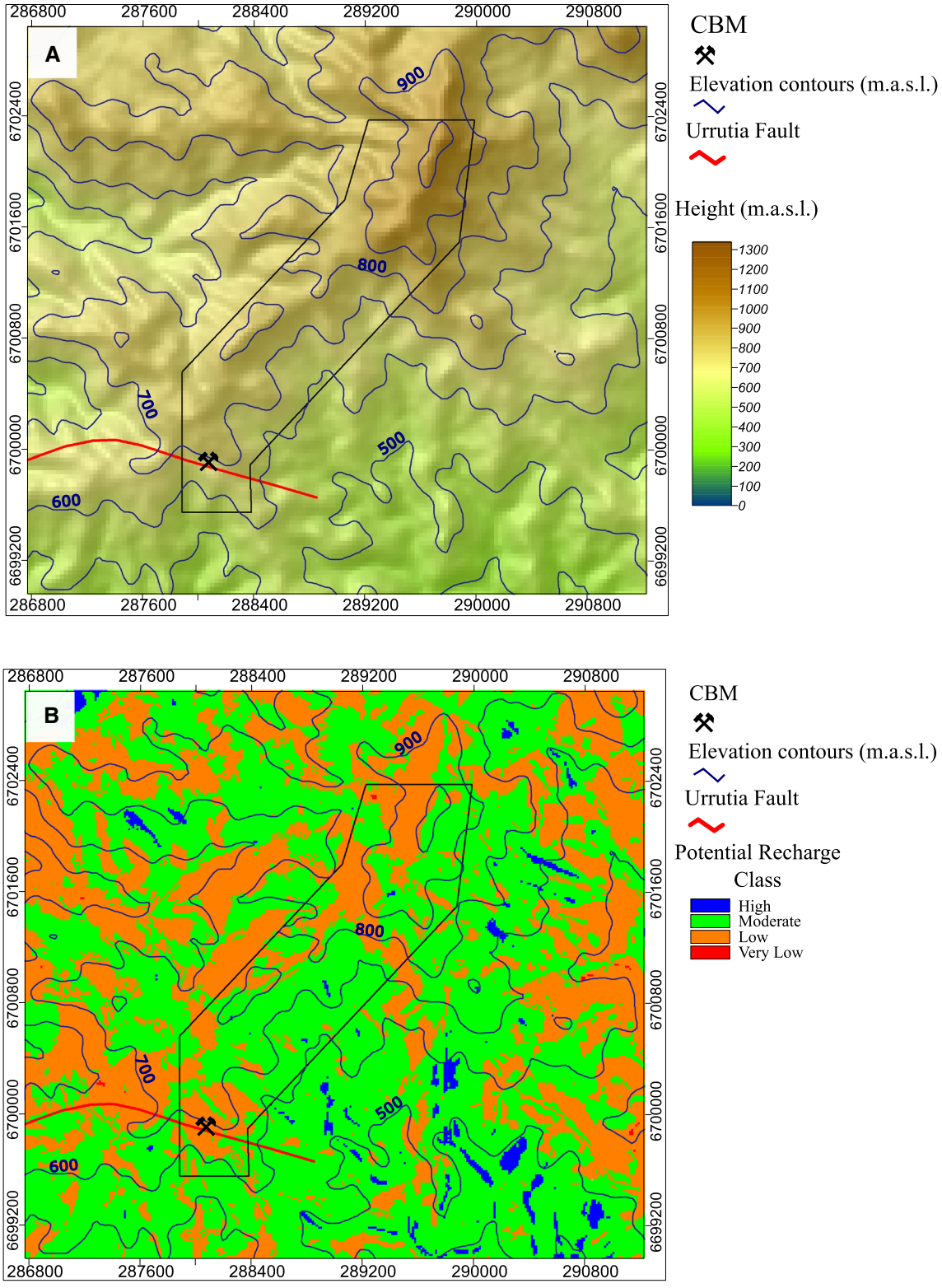

Fig. 9 Identification of the effective water intake area (black NE–SW elongated polygon) for the Brillador Mine projected onto the recharge potential map

overall direction of groundwater flow, is hypothesized to have a barrier effect on lateral groundwater migration. Quantitative assessment of the differential head across the main faults of the study area is still required; however, by analogy to other sites, we propose that this fault impounds recharge and possibly channels flow into the open (flooded) CBM workings below the 500 level. In summary, our conceptual model proposes that infiltration enters the mountain block at higher elevations, principally through high-permeability fracture zones associated with low storage (i.e. thin soil cover) and moves rapidly through the fracture network to recharge the mountain-block aquifer. After arriving at the saturated zone, groundwater likely migrates down the hydrologic and topographic gradient toward the coastal aquifers, eventually discharging to the coastal plain. Also, on the basis of our observations in the study area and the findings of previous investigators, we estimate an overall recharge rate on the order of 5% of the average annual rainfall.

Although our study placed special emphasis on studying physical aspects of the mountain block groundwater process, the data collected also provides insight to chemistry processes. The groundwater sampled as part of the present study contained a relatively high concentration of dissolved constituents (including Cu, As, Mn, and Fe). The pH of the percolating fluids was near neutral (average pH 6.7), in contrast to the expected acidity that is generally associated with sulfide ore bodies. The surprisingly moderate pH of groundwater in the study area is attributed to the neutralizing effect of mafic andesitic rocks.

The lack of acid drainage has contributed to the technical and educational post-mining use of the CBM, which includes pilot tests of new wall mine supporting materials. Thus, the CBM facility constitutes a suitable site to study hydrogeological processes in an arid environment with shallow soils and underlying fractured rock masses. The benefit that this research designation could offer other non-active mines, in terms of scientific research such as the one herein described, could be considered when addressing mine closure and developing mine closure plans.

Acknowledgements This work was developed within the framework of the Conicyt/Programa Fondecyt Project 1150587 and the Water Resources and Environment Program (PRHIMA, for its acronym in Spanish) of the Department of Mining Engineering of the Universidad de La Serena, and Conicyt/Fondap/15130015 Center CRHIAM. The paper benefited from the comments of two anonymous reviewers, and the editorial suggestions of Dr. A. Maest.

References

Adinolfi R, Falgiani A, Parisse B, Petitta M, Spizzico M, Tallini M (2008) Chemical and isotopic (δ^{18O}‰, δ^{2}H‰, δ^{13}C‰, ^{222}Rn) multi-tracing for groundwater conceptual model of carbonate aquifer (Gran Sasso INFN underground laboratory—central Italy). J Hydrol 357:368–388

Araya A, Salfate H (2014) Recopilation of geologic, historic, and topographic information and modeling of the Brillador mine through Sketchup and Surpac Graduation work, Ingeniería de Ejecución en Minas, Universidad de La Serena **(in Spanish)**

Assirati L, Silva NR, Berton L, Lopes AA, Bruno OM (2014) Performing edge detection by Difference of Gaussians using q-Gaussian kernels. J Phys Conf Ser. https://doi.org/10.1088/1742-6596/490/1/012020

Babiker M, Gudmundsson A (2004) The effects of dykes and faults on groundwater flow in an arid land: the Red Sea Hills, Sudan. J Hydrol 297:256–273

Bachmair S, Weiler M (2012) Hillslope characteristics as controls of subsurface flow variability. Hydrol Earth Syst Sci 16:3699–3715

Brodsky EE, Roeloffs E, Woodcock D, Gall I, Manga M (2003) A mechanism for sustained groundwater pressure changes induced by distant earthquakes. J Geophys Res Sol Earth 108(B8):2390

Buchtele J, Curda S, Hrkal Z, Krasny J (2003) New approach to using GIS in groundwater runoff assessment: the Krusne Mts. In: Krasny J, Hrkal Z, Bruthans J (eds) Proceedings, International Conference on Groundwater in Fractured Rocks Prague Czech Republic, Prague. IHP-VI, Series in Groundwater 7. International Association of Hydrogeologists, pp 135–136

Caine JS, Evans JP, Forster CB (1996) Fault zone architecture and permeability structure. Geology 24:1025–1028

Chander G, Markham BL, Helder DL (2009) Summary of current radiometric calibration coefficients for Landsat MSS, TM, ETM+, and EO-1 ALI sensors. Remote Sens Environ 113(5):893–903

Chavez PS (1996) Image-based atmospheric corrections-revisited and improved. Photogramm Eng Rem S 69(9):1025–1036

CIREN (2004) Determination of homogeneous zones of groundwater availability between the Elqui, Limarí and Choapa rivers. http://bibliotecadigital.ciren.cl/handle/123456789/1193. Accessed 13 April 2016 **(in Spanish)**

Cizdziel JV, Wei Y, Stetzenbach KJ, Hodge VF, Cline J, Howley R, Phillips FM (2008) Recent measurements of 36Cl in Yucca Mountain rock, soil and seepage. J Radioanal Nucl Chem 275:133–144

Conrad O, Bechtel B, Bock M, Dietrich H, Fischer E, Gerlitz L, Wehberg J, Wichmann V, Böhner J (2015) System for automated geoscientific analyses (SAGA) v. 2.1.4. Geosci Model Dev 8:1991–2007

Cooper HH, Bredehoeft JD, Papadopulos IS, Bennett RR (1965) The response of well-aquifer systems to seismic waves. J Geophys Res 70(16):3915–3926

Dar IA, Sankar K, Dar M (2010) Remote sensing technology and geographic information system modeling: an integrated approach towards the mapping of groundwater potential zones in hardrock terrain, Mamundiyar basin. J Hydrol 394:285–295

Dubo A (1984) Geologic information and perspectives for the Brillador mine (29°48′S/71°11′W). Graduation work, Ingeniería de Ejecución en Minas, Universidad de La Serena, La Serena, Chile, pp 41 **(in Spanish)**

Emparán C, Pineda F (2000) Geologic Map No 18, La Serena-La Higuera Area, 1:100.000. Servicio Nacional de Geología y Minería, Santiago, Chile

Evans JP, Forster CB, Goddard JV (1997) Permeability of fault-related rocks, and implications for hydraulic structure of fault zones. J Struct Geol 19(11):1393–1404

Hengl T, Heuvelink GB, Van Loon EE (2010) On the uncertainty of stream networks derived from elevation data: the error propagation approach. Hydrol Earth Syst Sci 7(1):767–799

Iwatsuki T, Furue R, Mie H, Ioka S, Mizuno T (2005) Hydrochemical baseline condition of groundwater at the Mizunami underground research laboratory (MIU). Appl Geochem 20:2283–2302

King CY, Azuma S, Igarashi G, Ohno M, Saito H, Wakita H (1999) Earthquake-related water-level changes at 16 closely clustered wells in Tono, central Japan. J Geophys Res 104(B6):13073–13082

Kuntz J (1925) Mining Monography of the Coquimbo Province. Booklet 13. Cuerpo de Ingenieros de Minas, Santiago

Lee S, Wolberg G, Shin SY (1997) Scattered data interpolation with multilevel B-splines. IEEE T Vis Comput Gr 3(3):228–244

Llaumett C (1970) Santa Rosita and 26 de Agosto geologic map, Brillador District, Coquimbo, Chile. In: UNDP-Empresa Nacional de Minería, 1971, Report of the Chile 28 Project

Maksaev V, Townley B, Palacios C, Camus F (2007) Metallic ore deposits. In: Moreno T, Gibbons W (eds) The geology of Chile, Chap 6. The Geological Society of London, pp 179–200

Matsushita B, Yang W, Chen J, Onda Y, Qiu G (2007) Sensitivity of the enhanced vegetation index (EVI) and normalized difference vegetation index (NDVI) to topographic effects: a case study in high-density cypress forest. Sensors 7(11):2636–2651

Minnaert M (1941) The reciprocity principle in lunar photometry. Astrophys J 93:403–410

Montecinos E (1982) Effect of exposure on the development of Aridosls in the IV Region. Graduation work, Ingeniería Agronómica, Universidad de Chile, Santiago, Chile, pp 79 **(in Spanish)**

O'Callaghan JF, Mark DM (1984) The extraction of drainage networks from digital elevation data. Comput Vision Graph 28(3):323–344

Oyarzun R, Oyarzún J, Lillo J, Maturana H, Higueras P (2007) Mineral deposits and Cu–Zn–As dispersion–contamination in stream sediments from the semiarid Coquimbo Region, Chile. Environ Earth Sci 53:283–294

Paskoff R (1993) Semi-arid Chile geomorphology. Departamento de Publicaciones, Universidad de La Serena. La Serena, Chile

Petro AB, Sbert C, Morel J (2014) Multiscale retinex. Image Process Line 4:71–88. https://doi.org/10.5201/ipol.2014.107

Prassad RK, Mondal NC, Banerjee P (2008) Deciphering potential groundwater zone in hard rock through the application of GIS. Environ Earth Sci 55:467–475

Rice EW, Baird RB, Eaton AD, Clesceri LS (2012) Standard methods for the examination of water and wastewater. American Public Health Assoc, Washington, DC

Rouse JW, Haas RH, Schell JA, Deering DW (1974) Monitoring vegetation systems in the Great Plains with ERTS. In: Proc, 3rd Earth Resources Technology Satellite-1 Symp, Greenbelt, USA; NASA SP-351, pp 3010–3017, https://ntrs.nasa.gov/archive/nasa/casi.ntrs.nasa.gov/19740022614.pdf. Accessed 12 Sept 2017

Scanlon BR, Keese KE, Flint AL, Flint LE, Gaye CB, Edmunds WM, Simmers I (2006) Global synthesis of groundwater recharge in semiarid and arid regions. Hydrol Process 20:3335–3370

Shaban A, Khawlie M, Abdallah C (2006) Use of remote sensing and GIS to determine recharge potential zones: the case of Occidental Lebanon. Hydrogeol J 14:433–443

Shelp ML, Zhan G, Upton B (2011) The applications of satellite based remote sensing techniques in the hydrological assessment of mine water supply and management systems. Mine Water Environ 30:242–251

Singh P, Krishana J, Kumar S (2013) Delineating groundwater potential zones in a hard-rock terrain using geospatial tool. Hydrolog Sci J 58(1):213–223

Smith JA, Tzeu LL, Ranson KJ (1980) The Lambertian assumption and landsat data. Photogramm Eng Rem Sensing 46(9):1183–1189

Smith SE, El-Shamy I, Abd-El Monsef H (1997) Locating regions of high probability for groundwater in the Wadi El-Arish Basin, Sinai, Egypt. J Afr Earth Sci 25(2):253–262

Squeo FA, Aravena R, Aguirre E, Pollastri A, Jorquera CB, Ehleringer JR (2006) Groundwater dynamics in a coastal aquifer in north-central Chile: implications for groundwater recharge in an arid ecosystem. J Arid Environ 67:240–254

Tweed SO, Leblanc M, Webb JA, Lubczynski MW (2007) Remote sensing and GIS for mapping groundwater recharge and discharge areas in salinity prone catchments, southeastern Australia. Hydrogeol J 15:75–96

Zambra J (2015) Geotechnical characterization of the 580 level, Brillador mine. Unpublished internal technical report, Mines Engineering Department, Universidad de La Serena, pp 34 **(in Spanish)**

Zhao G, Gao J, Tian P, Tian K (2009) Comparison of two different methods for determining flow direction in catchment hydrological modeling. Water Sci Eng 2(4):1–15